Studies on Microscopic Structure of Sol−Gel Derived Nanohybrids Containing Heteropolyacid

Takayuki Nakanishi,[†] Tomohisa Norisuye,*[,†] Haruyoshi Sato,[†] Tsuyoshi Takemori,[†] Qui Tran-Cong-Miyata,[†] Toshiya Sugimoto,[‡] and Shigeki Nomura[‡]

Department of Macromolecular Science and Engineering, Graduate School of Science & Technology, Kyoto Institute of Technology Matsugasaki, Sakyo-ku, Kyoto 606-8585, Japan, and R&D Center, Sekisui Chemical Co., Ltd., 32 Wadai, Tsukuba-shi, Ibaraki 300-4292, Japan

Received March 14, 2006; Revised Manuscript Received March 20, 2007

ABSTRACT: The microscopic structure of organic−inorganic hybrid membranes containing heteropolyacid has been investigated by atomic force microscopy (AFM), small-angle X-ray scattering (SAXS), and Fourier transform infrared spectroscopy (FT-IR). The hybrids were prepared by hydrolysis and condensation reactions, the so-called sol−gel reaction of 1,8-bis(triethoxysilyl)octane (TES-Oct) in the presence of phosphotungstic acid (PWA) with hydrated water. The characteristic lengths evaluated by using AFM and SAXS revealed the evolution of the domain structures upon increasing PWA concentration. Thermogravimetric analysis (TGA) indicated that increasing PWA concentration led to remarkable increase in the characteristic temperature for a weight loss. By combination of analysis using TGA and FT-IR, it was found that highly condensed domains were disintegrated, leading to the formation of loose networks with defect structures in the vicinity of the characteristic temperature. Correspondingly, the organic bridge was further broken. Variation of the characteristic temperature with the PWA concentration was strongly correlated to the evolution of the interdomain distance and the surface characteristic length scales, which were respectively observed by SAXS and AFM. Such a well-developed ionic domain structure offered fairly good performance of the proton conductivity in range 10^{-4} to 10^{-2} (S/cm) in spite of the rigid matrix of the sol−gel network.

Introduction

The sol−gel method is a suitable technique to synthesize polymeric materials such as fibers, membranes, ceramics, and gels.[1] The sol−gel process involves two principal reactions consisting of (1) hydrolysis of alkoxides groups to form silanol groups and (2) subsequent condensation of silanol groups to produce siloxane bonds in alcohol/water solutions. The reaction is accelerated when acid or base catalysts are employed. Electrophilic characteristics, which are rapid hydrolysis and subsequent condensation, lead to a less-branched structure for acidic systems. On the other hand, highly branched silica colloids are obtained by slow hydrolysis and fast condensation, the characteristic of nucleophilic reaction for base-catalyzed systems.[2,3] In either case, the simple procedure and the low operation temperature of the sol−gel process have fascinated the materials science community. Because of the capability of polymer networks to trap small molecules, sol−gel-derived materials open a route of applications for catalyst support, molecular sieves, proton conducting membranes, and so on.

Phosphotungstic acid (PWA) belongs to a large group of heteropolyacids, which are strong inorganic acids.[4,5] PWA involves the Keggin structure consisting of a central P atom in tetrahedral coordination surrounded by 12 edge-sharing tungstic acid with the lattice cell parameter of 11.7 Å.[6] To neutralize the huge anion, PWA bears a large amount of hydrated water depending on the temperature and humidity. This particular structure exhibits exceptionally high proton conductivity because of the high mobility of hydrated water that is close to pure water.[7] Thus sol−gel-derived networks containing PWA are considered to be a good candidate for fuel cell membranes thanks to the high conductivity of PWA.

Tatsumisago et al. prepared PWA-dispersed silica membranes exhibiting the proton conductivity on the order of 10^{-4} to 10^{-3} S/cm.[8] Although the PWA-dispersed silica materials have great advantages such as thermostability and dimensional stability because the limit of the intake capacity of PWA for the conventional sol−gel network of tetraethoxysilane (TEOS) still remains at 47%, exploration of more suitable host which is capable of incorporating a larger amount of PWA without segregation is strongly demanded. To achieve this requirement, alkoxysilanes were organically modified with various organic spacers such as alkylene, alkyleneoxide, and isocyanato-alkyleneoxide.[9−23] Among them, a new class of precursors consisting of both organic and inorganic parts was proposed.[24−27] Such materials have the following advantages: (1) Organic−inorganic products can be obtained by one-step polymerization because each component is connected at monomer level. (2) The cyclization reaction of monomers between neighboring alkoxide groups can be fairly circumvented owing to the moderate separation distance determined by the length of organic spacer.[28] (3) The organic part provides better flexibility, dissipating energy concentrated at the rigid inorganic backbone.

General reaction schemes for bridged silsesquioxanes with various organic spacers are illustrated in Figure 1 (proton conductor is not drawn here). Provided that hydrolysis and condensation reactions for bridged-alkoxysilanes effectively proceed without any cyclization reaction, the resulting structure is characterized by a highly condensed cagelike structure (cubic silsesquioxanes) with defect structure.[29−31] The fraction of the cagelike structure is considered to be dependent on the catalysts, the experimental temperature, the length of organic groups, and the concentrations of reagents. Subsequently, the pre-gel clusters containing cage and/or network structures develop into a gel,

* To whom correspondence should be addressed. E-mail: nori@kit.ac.jp.
[†] Kyoto Institute of Technology.
[‡] Sekisui Chemical Co., Ltd.

10.1021/ma060573h CCC: $37.00
Published on Web 05/10/2007

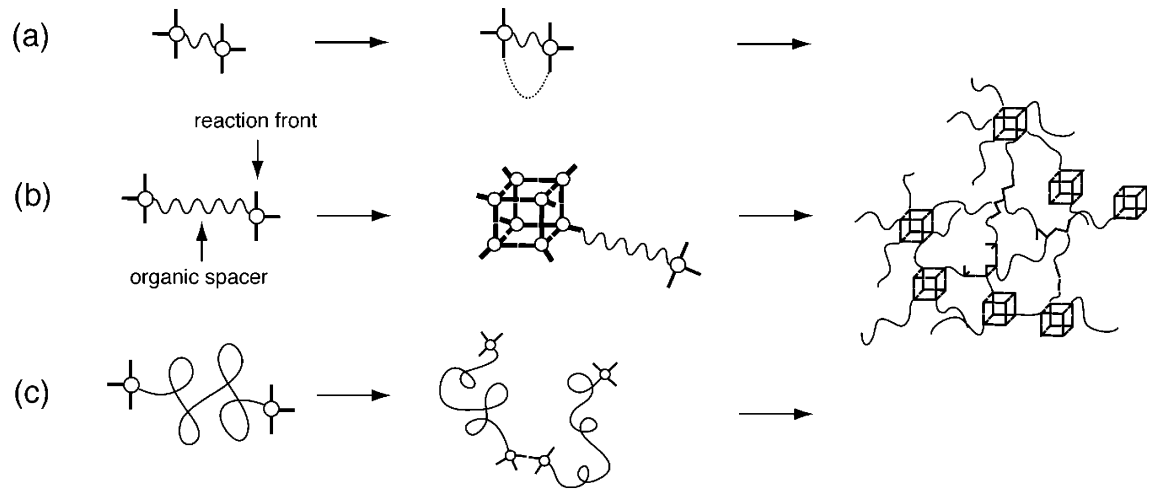

Figure 1. Schematic models for bridged silsesquioxanes with various organic spacers.

leading to an immobile solid with nano- or micrometer voids after removing diluents.

Because the better conduction takes place by effective exchange of protons, the concentration and degree of dissociation of PWA as well as the number of hydrated water are the crucial factors for designing proton-conducting membranes. However, even if we succeed to prepare an electrolyte membrane containing a large amount of conductors, disconnection of the transport channels caused by segregation and/or crystallization of conductors would lower the potential proton conductivity. On the contrary, water-containing clusters should be kept large enough to fulfill the percolation condition for the conductive phase. This means nanodispersed/homogeneous structures are not always an acceptable structure for maximizing functionalities of fuel membranes. In that sense, optimization of the hierarchical structure is necessary, and this demand can be satisfied by investigating the correlations among reactions, microscopic structure, and conducting properties. Therefore, we focused on investigation of microscopic structure for PWA-dispersed membranes with organically modified precursors by taking account of the role of both PWA and the hydrated water in the reaction and the structure of the membranes.

Experimental Section

Samples. 1,8-Bis(triethoxysilyl)octane (TES-Oct, Gelest), $(OC_2H_5)_3$-Si-$(CH_2)_8$-Si-$(OC_2H_5)_3$, phosphotungstic acid (PWA, Aldrich), $H_3PW_{12}O_{40}$, and isopropyl alcohol (IPA, Wako pure chemical industries) were used in this study. The reaction batch was prepared by adding the mixture (PWA + water + IPA) into the mixture (TES-Oct + IPA) to initiate the reaction. After vigorous stirring, the solution was filtered through a Teflon membrane with the pore size 0.25 μm and poured into a plastic petri dish, followed by an aging period for 24 h at 25 °C. After solidification, the obtained membranes were further aged under saturation vapor pressure at 60 °C for another 24 h. All of the samples were transparent, suggesting that no macroscopic phase separation (the scattering of visible light) occurs under our experimental conditions. The dried membranes were then carefully washed with and stored in distilled water prior to measurements. PWA concentrations were varied in the range [PWA]/[TES-Oct] = 0.01−0.25, while the concentration of TES-Oct was kept at 18.67%. For the higher PWA concentration, gelation took place so quickly that injection of the solution into a petri dish was not allowed within the limited mixing time. To estimate the amount of leaking PWA, the residual solution was titrated by a sodium hydroxide solution with a calibrated curve prepared by titration of the known amount of PWA. As a result, it was found that around 10−30 wt % of PWA remained in the membrane after washing. Although the leaked amount of PWA is not small, the remaining PWA provides sufficient pathway for the proton conduction as demonstrated below. Further noticeable leaking was not observed on repetitive washing. TES-Oct membranes catalyzed with 1N of hydrochloric acid was also prepared as a reference. Typical thickness of the sample was 200 μm. The membranes contains 30 wt % of water in the swollen state irrespective of the PWA concentration according to a separate water-uptake measurement.

Characterization. *Fourier Transform Infrared Spectroscopy (FT-IR).* FT-IR measurements were carried out on a Perkin-Elmer Spectrum GX system equipped with an attenuated total reflection (ATR) attachment. The ATR spectra were collected from 650 to 4000 cm^{-1} with a resolution of 4 cm^{-1}. The background spectra including the absorption of vapor and carbon dioxide were obtained by measuring the absorption of an empty ATR crystal used as reference.

Small-Angle X-ray Scattering (SAXS). SAXS measurements were performed on an X-ray diffraction instrument (Mac Science Co. Ltd., M18XHF22) equipped with a two-dimensional imaging plate detector, a high-flux Huxley−Holmes camera, and a nickel-filtered Cu Kα X-ray (24 mA, 50 kV, λ = 0.154 nm) at room temperature. The scattering intensities were accumulated for 1 h. The 1-D scattering functions were obtained by radial averaging of two-dimensional data after correction for the scattering volume and transmission.

Static Light Scattering (SLS). SLS experiments were carried out by a DYNA-3000 polymer dynamics analyzer (Otsuka Electronics Co., Japan) equipped with a light source (5 mW He−Ne Laser) and an area detector (CCD) of 512 × 512 pixels. When the detector angle was set to zero, an isotropic scattering profile was obtained on the two-dimensional detector with the scattering angle range ± 20°. In this case, the 1-D scattering functions were obtained by radial averaging of two-dimensional data similar to the SAXS analysis. It is noted that one can acquire the higher scattering angle data (maximum 130°) by rotating the detector, although improvement of the data quality by the radial averaging is not allowed in this specific case.

Atomic Force Microscopy (AFM). AFM was operated in tapping mode using a Digital Instruments Multimode AFM, controlled by a Nanoscope IIIa scanning probe microscope controller with an extender module. A commercially available silicon tip with a spring constant of 30−40 N/m, single beam cantilevers of 125 μm long, and a typical radius of curvature in the range 5−10 nm was used at resonance frequencies ranging from 310 to 340 kHz depending on cantilever. Both topography and phase images with various scan sizes 500, 1000, 2000, and 4000 nm were collected using tapping mode with a scan rate of 1 Hz in ambient atmosphere at room temperature. These images were transformed into a single master curve of the power spectrum after second-order background subtraction, fast Fourier transform (FFT), and radial averaging by

homemade software. Because the thickness of the sample is more than 80 μm, the AFM results are free from the substrate surface.

Thermogravimetric Analysis (TGA). Thermogravimetric analysis (TGA) was conducted using a TGA2950 (TA Instruments thermogravimetric analyzer) with high-resolution mode. Sample weight was in the range of 5−9 mg. Nitrogen was used as a purge gas. The heating rate was dynamically varied in response to the changes in the decomposition rate of the sample so as to improve the resolutions of the weight change. Maximum ramp heating rate was set at 20 °C/min.

Conductivity Measurement. Proton conductivity measurements were performed on a Hioki 3532−80 impedance analyzer coupled with two platinum electrodes placed in a thermostat chamber (Espec Co. Ltd, LHL-113) at 80 °C/95% RH. The conductivity was determined from Cole−Cole plot by an AC impedance method in the range 10 Hz to 1 MHz. The measurements were iteratively carried out until the impedance reached the plateau value.

Data Analysis. *AFM.* To obtain the spatial correlation length from AFM topography images, power spectral density (PSD) functions were calculated by two-dimensional Fourier transformations of topography images as

$$I(q_x,q_y) = \frac{1}{L^2}\left|\int_0^L \int_0^L (z(x,y) - \bar{z}) \exp[-i(q_x x + q_y y)]\, \mathrm{d}x\, \mathrm{d}y\right|^2 \quad (1)$$

where L is the image size, q_x and q_y are the wave vector along the x and y axes, and $\bar{z}$ is the mean height. The 2D-PSD is further transformed into polar coordinates by averaging over azimuthal angle ϕ by

$$I(q) = \frac{1}{2\pi}\int_0^{2\pi} I_{2D}(q_x,q_y,\phi)\, \mathrm{d}\phi \quad (2)$$

Note that $I(q)$ is equivalent to the Fourier transformation of the real space height−height correlation function, $G(r)$.[32] As explained in the Appendix, $I(q)$ exhibits the following asymptotic behavior:

$$I(q) = \begin{cases} k_0 q^{-2(1+2\alpha)} & \text{for } q \gg \xi \\ k_1 q^{-\beta} & \text{for } q \ll \xi \end{cases} \quad (3)$$

In this study, the following form is used to estimate ξ.

$$I(q) = \frac{1}{k_0(\xi q)^{2(1+2\alpha)} + k_1(\xi q)^{\beta}} \quad (4)$$

This equation exhibits the asymptotic power law behavior with the exponents $-2(1 + 2\alpha)$ for the large q and $-\beta$ for the smaller q regions, respectively. This enables us to determine ξ by a nonleast-squares fitting procedure.

Results and Discussion

FT-IR is a powerful tool to observe the specific chemical structure of PWA and the interaction between PWA and hydrated water. Figure 2 shows the absorption spectra of PWA in the solid state. The spectra exhibit absorption peaks in the region of 3800−1200 and 1150−650 cm^{-1}, which correspond to the vibration modes of water and PWA, respectively. Those absorption bands, νOH−H_2O (3400−3500 cm^{-1}), νOH−$H_2O_5^+$ (3180 cm^{-1}), δOH− $H_2O_5^+$ (1720 cm^{-1}), δOH−H_2O (1620 cm^{-1}), νP−O (1078 cm^{-1}), νW═O (970−980 cm^{-1}), νW−O_b−W (880−910 cm^{-1}), νW−O_c−W (770−780 cm^{-1}), have already been assigned in the literature.[33] In the following, those are used to confirm that PWA preserving the native Keggin structure is successfully incorporated in the membranes.

Figure 3 represents the FT-IR spectra for the TES-Oct/PWA membranes, where the strong peaks appeared at 2926 and 2857 cm^{-1} were assigned to the absorption of the methylene groups of the organic bridges (Figure 3a). It was confirmed that the peak intensity increased with increasing length of the organic bridges in organic−inorganic precursors. The absorbance peaks associated with the organic bridge were used as internal reference to compare a series of FTIR data because they were free from the interaction with PWA.

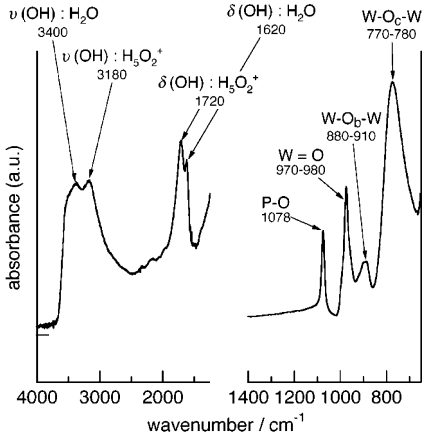

Figure 2. FT-IR spectrum for PWA.

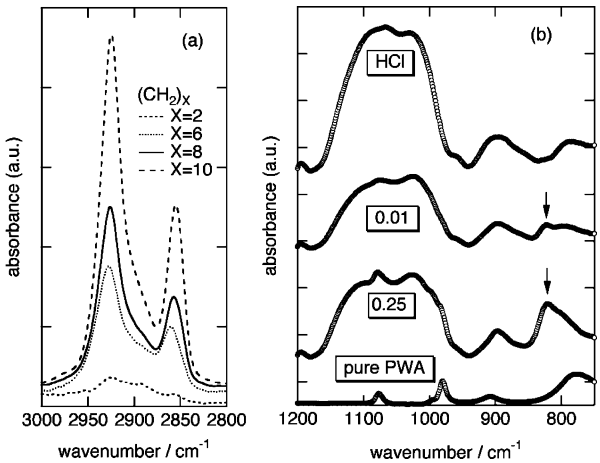

Figure 3. (a) FT-IR spectra for the sol−gel derived hybrids with different organic spacer lengths and (b) FT-IR spectra for pure PWA, the TES-Oct membranes catalyzed by HCl, and by PWA with [PWA]/[TES-Oct] = 0.01 and 0.25.

The absorption peaks that appeared in the range of 1400−650 cm^{-1} are related to Si−O−Si linkage. The asymmetric stretching band of P═O would be the best to confirm the existence of PWA in the hybrid membranes because the signal from heteroatom P is shielded by 12 tungstic acid units in its neighbors and is free from the interaction unlike the outer W═O groups. However, the absorption band unfortunately overlapped with that of Si−O−Si linkage. Similar overlap was also found for the symmetric stretching band of W−O_b−W, which appeared from 970 to 980 cm^{-1}. In contrast, the specific band for PWA was found at 820 cm^{-1}. Figure 3b shows representative absorption spectra with different PWA concentrations. Although the characteristic band for W−O_c−W shifted from 780 to 820 cm^{-1}, noticeable increase in the intensity with the PWA concentration was found when the spectra for [PWA]/[TES-Oct] = 0.01 and 0.25 were compared as indicated by the solid arrows. The conclusion can be led by performing a nonlinear least-squares fit to a multi-Gaussian function with a polynomial background (not shown here).

Figure 4a shows the scattering functions obtained by SAXS for a series of the TES-Oct/PWA membranes as a function of the PWA concentration, where the signals behind the beam stopper were masked on the analysis. The scattering profiles were

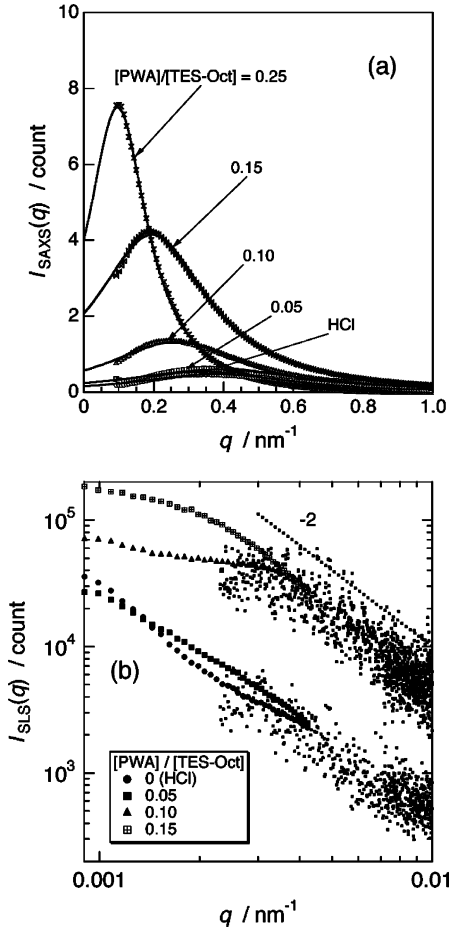

Figure 4. (a) SAXS and (b) SLS profiles for the TES-Oct membranes with different PWA concentrations.

characterized by an appearance of a peak, which shifts to lower q when increasing the PWA concentration. The solid lines were drawn for clarity. Because a similar scattering function was observed for a HCl-catalyzed membrane without PWA, it can be deduced that inverse of the peak position corresponds to the intervoid distance (or the interdomain distance of the hybrid clusters containing PWA) rather than the spatial correlation between the PWA-rich and -poor phases without voids. Note that PWA plays an additional factor for amplification of the total intensities for the PWA/silica system because the scattering contrast for SAXS increases with atomic number. The interdomain distances, ξ_{SAXS}, defined by

$$\xi_{SAXS} = 2\pi/q_{peak} \tag{5}$$

as a function of the PWA concentration is shown below, where q_{peak} indicates the peak position of the scattering intensity. While SAXS provides the intervoids structure, the distribution of PWA in the hybrid membranes is an important factor to study the microscopic structure of the hybrid membranes. Thus, a light-scattering experiment was carried out to investigate the microscopic structure on the length scale of visible light. The double-logarithmic plot of the scattering functions obtained by a two-dimensional scattering setup was shown in Figure 4b. Only the scattered intensities with the zero detector angle could result in sufficient quality after radial averaging of the two-dimensional data. Nevertheless, the slope of the scattering functions at the high-q region was -2, indicating the system was in one-phase regime and PWA was randomly dispersed in the network.

Figure 5 shows the surface topography of the TES-Oct/PWA membranes obtained by tapping-mode AFM with a scan size of 500 nm, where the obtained images were three-dimensionally reconstructed by homemade software to achieve better visualization. In our previous study, we reported that the TES-Oct cluster evolution for the PWA (strong acid) system was similar to that of base-catalyzed systems. Typical acid-catalyzed gels grew by extending the chain with less branching, whereas base-catalyzed gels were constructed from highly branched particles. Those topographies indicated that the membrane structure consisted of a large particle domain structure. Although the information was limited to the surface, more quantitative analysis based on the spatial correlation function was performed in order to compare the results with SAXS data in the following.

Figure 6 shows the power spectra of the AFM topography as a function of the PWA concentration. The spectra were obtained by 2-D FFT of the AFM topographies and subsequent radial average, followed by the superposition of the averaged spectra obtained with scanning sizes of 500, 1000, 2000, and 4000 nm. It was found that the spectra were characterized by two distinct power laws intercepting at a certain wave vector, ξ^{-1}, as indicated by the arrows in the figure. Curve fitting using eq 4 was satisfactory for all the spectra as indicated by the solid lines, leading to a quantitative evaluation of ξ. The deviation from the power law in the higher q regions is due to the limit of image resolution and the quantization on FFT. As a result, the inverse of the reciprocal correlation length seems to shift to a lower wave vector with increasing the PWA concentration.

Figure 7 shows the first-order derivative, dw/dT of the weight loss as a function of the PWA concentration obtained by using high-resolution TGA for the TES-Oct/PWA membranes. In the high-resolution mode of TGA, the initial heating rate of 20 °C/min was varied in response to the changes in the decomposition rate of the sample. As shown in the figure, the dramatic weight loss was found around 510 °C, which corresponds to the characteristic temperature, T_{TGA}, for thermal decomposition of the organic bridge. T_{TGA} increased with increasing PWA concentration, suggesting a systematic increase in the thermostability associated with the specific structure of the TES-Oct/PWA membranes.

To disclose the relation between the thermostability and the microscopic structure, FT-IR measurements were subsequently carried out under various destination temperatures. The absorp-

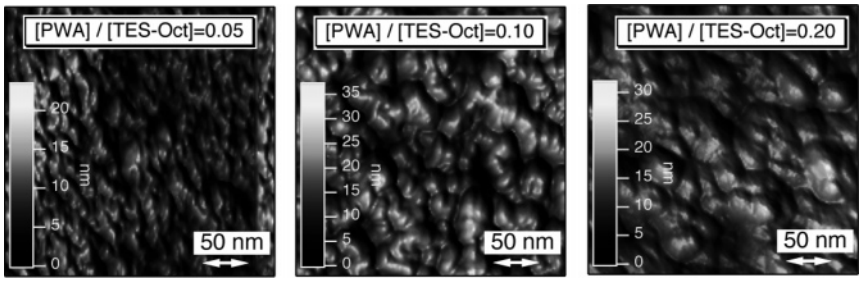

Figure 5. Surface topographies obtained by AFM with the scanning size of 500 nm for the TES-Oct membranes.

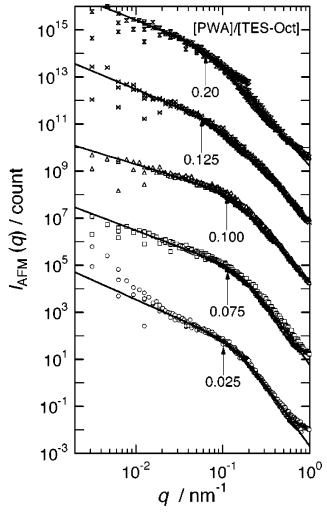

Figure 6. Power spectra obtained by 2-D FFT for the TES-Oct membranes with different PWA concentrations. The solid lines were obtained by fitting with eq 4.

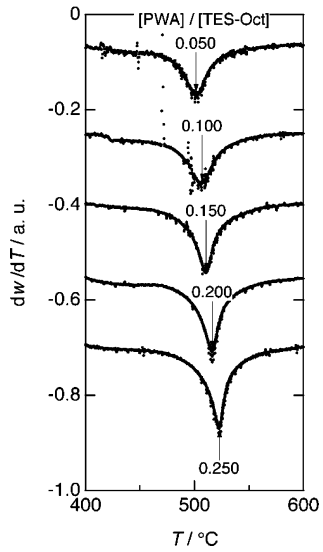

Figure 7. First-order derivatives of weight loss, dw/dT, as a function of the observation temperature, T, for the TES-Oct membranes.

tion band around 1130 cm^{-1}, which was assigned as the characteristic vibration of the cubic hydrogen-silsesquioxanes by Liu et al.,[29] disappeared upon thermal curing, whereas a new absorption peak in 1070 cm^{-1} associated to Si−O−Si network structure emerged simultaneously. In the case of methyl-silsesquioxanes, the Si−O−Si network absorption band shifted from 1130 to 1030 cm^{-1}, indicating effects of the side groups surrounding the cube. Figure 8 represents the FT-IR spectra of the TES-Oct membranes catalyzed by (a) HCl and (b) PWA. In the former case, the intensities for the Si−O−Si linkage associated with the cagelike structure decreased with increasing temperature. The stretching mode of the organic bridge disappeared correspondingly. It is speculated from this combination analysis that the cagelike structure is necessary to maintain the thermostability of the organic−inorganic hybrids. Decomposition of the organic bridge associated with disintegration of the cagelike structure was also found for the TES-Oct membranes containing PWA, as shown in Figure 8b. For the PWA-dispersed membranes, the thermostability is significantly improved owing to the presence of larger domains with highly condensed cagelike structure. Note that the "presence" of PWA in hybrid matrix as a filler played a minor role on the thermostability because it was confirmed that the characteristic temperature did not correspond to incorporated amount of PWA in the membrane, which will be reported in the forthcoming paper.

As shown above, the cagelike structure in the TES-Oct membranes is disintegrated into the network structure with defects upon increasing temperature. Figure 9 shows the FT-IR spectra for the PWA-containing sol−gel-derived membranes prepared by tetraethoxysilane (TEOS) and TES-Oct observed at room temperature, where the TES-Oct membrane was tested after a thermal treatment at 700 °C, which is located well above the characteristic temperature for the cage disintegration. As found from the figure, the FT-IR spectra for the TEOS membranes are quite similar to that for the TES-Oct aged at 700 °C in the range 1000−1300 cm^{-1}. Because the TEOS membranes have no organic spacer, the structure more likely involves intra-cross-linking structure, leading to a predominant network with defect rather than a cagelike structure.

The results of AFM characteristic length ξ_{AFM}, the interdomain distance ξ_{SAXS}, and the characteristic temperature T_{TGA},

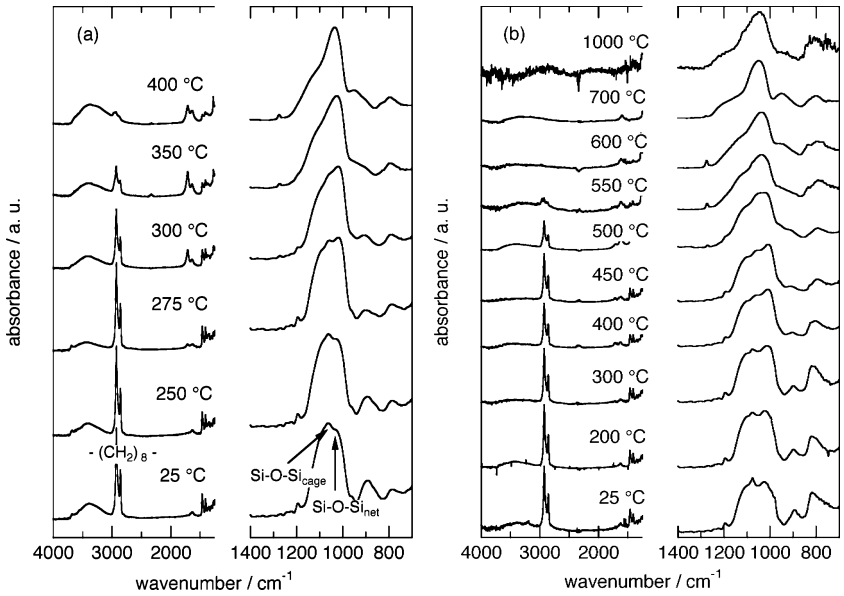

Figure 8. FT-IR spectra for the TES-Oct membranes catalyzed by (a) HCl and (b) PWA. The spectra were acquired after TGA experiments under different destination temperatures.

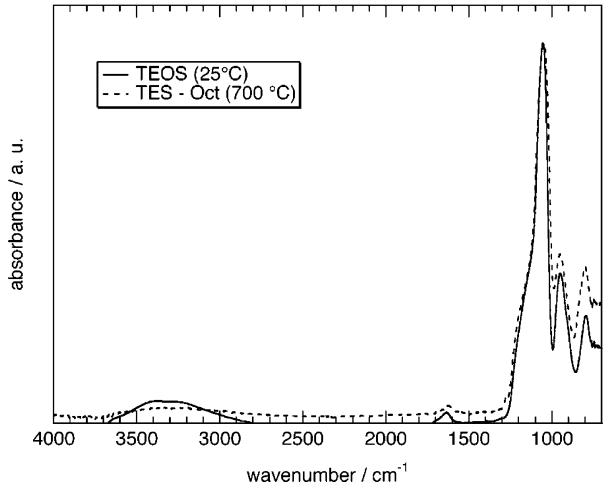

Figure 9. Comparison of the FT-IR spectra between the TEOS and TES-Oct membranes where the TES-Oct membrane was tested after a thermal treatment at 700 °C.

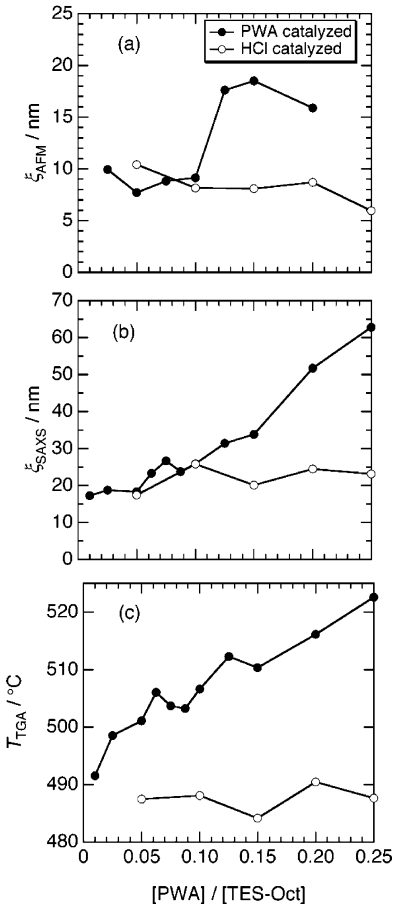

Figure 10. ξ_{AFM}, ξ_{SAXS}, and T_{TGA} as a function of the PWA concentration for the TES-Oct membranes. The open symbol exhibited the results of the HCl-catalyzed membranes as a reference.

were summarized as a function of the PWA concentration, [PWA]/[TES-Oct], in Figure 10a−c. ξ_{AFM}, ξ_{SAXS}, and T_{TGA} systematically increased with increasing [PWA]/[TES-Oct]. Because the amount of water also increased with the PWA concentration, ξ_{AFM} for the HCl-catalyzed membranes were also exhibited in the figure. As a result, the structural evolution was found only in the PWA-catalyzed membrane, suggesting the unique performance of PWA as a strong acid catalyst. While systematic variations were found in those data, the AFM data did not perfectly appear to track the SAXS data. This uncertainty

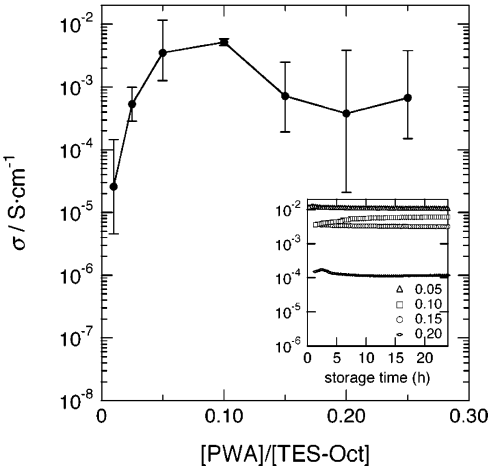

Figure 11. Proton conductivity of the TES-Oct membranes as a function of the PWA concentration. The inset shows the change in conductivities with storage time.

may be generated by additional contribution from the larger-scale structure, indicating the multifractal surface as described in the previous section.

Finally, Figure 11 shows the proton conductivity σ for a series of the TES-Oct/PWA membranes obtained by an AC impedance method at 80 °C. Despite the fact that those membranes were glassy and tightly cross-linked via the sol−gel method, σ exhibited fairly high values of 10^{-4} to 10^{-2} (S/cm) in our experimental range. The inset of the figure shows the change in conductivities with storage time. As a result, it was found that the hybrid membranes were fairly stable over 24 h in the experimental condition.

Conclusions

Generating and controlling hierarchal structure is one of the most important strategies to optimizing the functionality of advanced materials. In the case of proton-conducting membranes, the ionic domain structure should be maintained continuously and be large enough to achieve the percolation condition indispensable for high proton conduction. In general, macroscopic phase separation must be circumvented. Isolation of the proton conductor can be prevented by inducing gelation earlier than macroscopic phase separation because cross-linking has an important role in suppressing the concentration fluctuations and to fix the required structure. In that sense, sol−gel-derived hybrids containing phosphotungstic acid (PWA) studied here is a promising candidate.

Organic−inorganic polymer hybrids were prepared by sol−gel reaction of 1,8-bis(triethoxysilyl)octane (TES-Oct) in the presence of PWA. The surface characteristic length ξ_{AFM}, the interdomain distance ξ_{SAXS}, and the characteristic temperature for the weight loss T_{TGA} were evaluated respectively by using atomic force microscopy (AFM), small-angle X-ray scattering (SAXS), and thermogravimetric analysis (TGA), and a strong correlation was found among them. The characteristic parameters, ξ_{AFM}, ξ_{SAXS}, and T_{TGA} for the PWA-containing hybrid membranes increased with the PWA concentration, suggesting the systematic evolution of the domain structure without macrophase separation. Combining analysis using both FT-IR and TGA disclosed that the thermostability of the organic−inorganic hybrids was determined by the amount of the cage formed within the network, which was produced by effective reaction with a moderate organic spacer.

It was found that the potential of PWA as a catalyst was unleashed when PWA contains a sufficient amount of hydrated

water for the reaction, i.e., PWA were used as received. However, when HCl with the corresponding amount of water was employed as a catalyst, systematic evolution of the domain size was not observed, suggesting that the concentration of water plays a minor role, particularly for our experimental conditions.

Acknowledgment. This work is supported by Grant-in-Aid, no. 16750189 from the Ministry of Education, Science, Sports, Culture, and Technology.

Appendix

To characterize the surface structure, the height−height correlation function,[32]

$$G(r) \equiv \langle (z(r) - z(0))^2 \rangle = 2\langle z(r)^2 \rangle - 2\langle z(r)z(0) \rangle \quad \text{(A1)}$$

is calculated where $z(x)$ is the nominal height at position x. r corresponds to the distance between two arbitrary points. $G(r)$ may be calculated by averaging 1-D height−height correlation functions along the fast-scan x-axis of AFM,[34]

$$G(r) = \frac{1}{N}\sum_{i=1}^{N} \frac{1}{N - r/d} \sum_{j=1}^{N - r/d} [z(r + jd,id) - z(jd,id)]^2 \quad \text{(A2)}$$

where N, L, and d are the number of pixels along the x-axis, the scan size, and the unit length given by L/N, respectively. If there is no correlation on the surface, eq A1 becomes,

$$G(r) = 2[\langle z(r)^2 \rangle - \langle z(r) \rangle^2] = 2w^2 = \text{const} \quad \text{(A3)}$$

where w is the root-mean-square (rms) defined by,

$$w^2 \equiv \langle (z(r) - \langle z(r) \rangle)^2 \rangle \quad \text{(A4)}$$

By applying a Gaussian model,[35] eq A1 may be expressed by

$$G(r) = 2[w^2 - g(r)] = 2w^2\left[1 - \exp\left\{-\left(\frac{r}{\xi}\right)^{2\alpha}\right\}\right] \quad \text{(A5)}$$

where $g(r)$ is the pair correlation function defined by,

$$g(r) \equiv \langle \{z(r) - \langle z(r) \rangle\}\{z(0) - \langle z(r) \rangle\} \rangle \quad \text{(A6)}$$

Here α is an exponent representing the self-affinity of the rough surface with $0 \leq \alpha \leq 1$.[34] Eq A5 has the following asymptotic behavior,

$$G(r) = \begin{cases} 2w^2(r/\xi)^{2\alpha} & r \ll \xi \\ 2w^2 & r \gg \xi \end{cases} \quad \text{(A7)}$$

A Fourier transform of eq A7 gives,

$$A_{1D}(q) = \begin{cases} k_0 q^{-(1+2\alpha)} & q \gg \xi \\ A_{1D}(0) & q \ll \xi \end{cases} \quad \text{(A8)}$$

For q much larger than ξ^{-1}, the spectra exhibit a power law decay with an exponent $-(1 + 2\alpha)$. As the length scale becomes larger (i.e., q decreases), the intensities level off at a certain q corresponding to the inverse of the characteristic length, ξ. Therefore, ξ may be evaluated by an intersection of the power law and the level-off line as,[36]

$$\xi = \exp\left[\frac{\ln k_0 - \ln\{A_{1D}(0)\}}{1 + 2\alpha}\right] \quad \text{(A9)}$$

However, as pointed out in the literature,[35] lack of the sampling number for the correlated system leads to emergence of unexpected periodical cycles in $G(r)$ known as an artifact. To increase accuracy of the data, we directly performed a 2-D Fourier transform of AFM topographies for isotropic images rather than averaging of correlation functions. The power spectra with various scanning size were then calculated by radially averaging the 2-D FFT images, and the results were superimposed on each other without using any shift factor. It was found that the intensities obey the following scaling law.

$$I_{2D}(q) = A_{1D,x}(q_x)A_{1D,y}(q_y) \sim \begin{cases} k_0 q^{-2(1+2\alpha)} & q \gg \xi \\ I_{2D}(0) & q \ll \xi \end{cases} \quad \text{(A10)}$$

In our case, however, due to the presence of the larger-scale structures in AFM topography, indispensable contribution from the low-q intensity was observed as a finite slope. Such a behavior is known as "multifractal", which is discussed in the literature[32] and may be expressed by an additional power law function with an exponent $\beta < 2(1 + 2\alpha)$:

$$I_{2D}(q) = \begin{cases} k_0 q^{-2(1+2\alpha)} & \text{for } q \gg \xi \\ k_1 q^{-\beta} & \text{for } q \ll \xi \end{cases} \quad \text{(A11)}$$

Again, ξ may be estimated from the intersection of the two lines corresponding to $q \gg \xi$ and $q \ll \xi$ in the double-logarithmic plot of eq A11, where ξ can be expressed by,

$$\xi = \exp\left[\frac{\ln\{k_0/k_1\}}{2(1 + 2\alpha) - \beta}\right] \quad \text{(A12)}$$

Because some uncertainties are associated with the analysis using eqs A11 and A12, the following equation may be used to estimate ξ with greater quantification.

$$I_{2D}(q) = \frac{1}{k_0(\xi q)^{2(1+2\alpha)} + k_1(\xi q)^{\beta}} \quad \text{(A13)}$$

References and Notes

(1) Brinker, C. J.; Scherer, G. W. *Sol−Gel Science*; Academic Press: London, 1990.
(2) Yamane, M.; Inoue, S.; Yasumori, A. *J. Non-Cryst. Solids* **1984**, *63*, 13.
(3) Norisuye, T.; Inoue, M.; Shibayama, M.; Tamaki, R.; Chujo, Y. *Macromolecules* **2000**, *33*, 500.
(4) Pope, M. T. *Heteropoly and Isopoly Oxometalates*; Springer-Verlag: Berlin, 1983.
(5) Moffat, J. B. *Metal-Oxygen Clusters: The Surface and Catalytic Properties of Heteropoly Oxometalates*; Kluwer Academic/Plenium Publishers: New York, 2001.
(6) Song, I. K.; Kaba, M. S.; Barteau, M. A. *Langmuir* **2002**, *18*, 2358.
(7) Mohapatra, S. K.; Boyd, G. D.; Storz, F. G.; Wagner, S. *J. Electrochem. Soc.* **1979**, *126*, 805.
(8) Tatsumisago, M.; Honjo, H.; Sakai, Y.; Minami, T. *Solid State Ionics* **1994**, *74*, 105.
(9) Honma, I.; Nomura, S.; Nakajima, H. *J. Membr. Sci.* **2001**, *185*, 83.
(10) Lavrencic Stangar, U.; Groselj, N.; Orel, B.; Colomban, P. *Chem. Mater.* **2000**, *12*, 3745.
(11) Aoki, Y.; Norisuye, T.; Tran-Cong-Miyata, Q.; Nomura, S.; Sugimoto, T. *Macromolecules* **2003**, *36*, 9935.
(12) Honma, I.; Nakajima, H.; Nakajima, O.; Sugimoto, T.; Nomura, S. *Solid State Ionics* **2003**, *162−163*, 237.
(13) Honma, I.; Nakajima, H.; Nishikawa, O.; Sugimoto, T.; Nomura, S. *J. Electrochem. Soc.* **2002**, *149*, 1389.
(14) Honma, I.; Nakajima, H.; Nishikawa, O.; Sugimoto, T.; Nomura, S. *J. Electrochem. Soc.* **2003**, *150*, 616.
(15) Honma, I.; Nakajima, H.; Nomura, S. *Solid State Ionics* **2002**, *154−155*, 707.
(16) Honma, I.; Takeda, Y.; Bae, J. M. *Solid State Ionics* **1999**, *120*, 255.
(17) Kim, J.; Honma, I. *Electrochim. Acta* **2003**, *48*, 36338.
(18) Kim, J.; Honma, I. *Electrochim. Acta* **2004**, *49*, 3179.
(19) Kim, J.; Honma, I. *Electrochim. Acta* **2004**, *49*, 3429.

(20) Kim, J.; Honma, I. *Solid State Ionics* **2005**, *176*, 547.
(21) Lavrencic Stangar, U.; Groselj, N.; Orel, B.; Schmitz, A.; Colomban, P. *Solid State Ionics* **2001**, *145*, 109.
(22) Nakajima, H.; Honma, I. *Solid State Ionics* **2002**, *148*, 607.
(23) Nakajima, H.; Nomura, S.; Sugimoto, T.; Nishikawa, S.; Honma, I. *J. Electrochem. Soc.* **2002**, *149*, 953.
(24) Shea, K. J.; Loy, D. A. *Chem. Mater.* **2001**, *13*, 3306.
(25) Fan, H.; Reed, S.; Baer, T.; Schunk, R.; Lopez, G. P.; Brinker, C. J. *Microporous Mesoporous Mater.* **2001**, *44*−*45*, 625.
(26) Corriu, R. J. P.; Moreau, J. J. E.; Thepot, P.; Man, M. W. C. *Chem. Mater.* **1996**, *8*, 100.
(27) Loy, D. A.; Beach, J. V.; Baugher, B. M.; Assink, R. A. *Chem. Mater.* **1999**, *11*, 3333.
(28) Loy, D. A.; Carpenter, J. P.; Alam, T. M.; Shaltout, R.; Dorhout, P. K.; Greaves, J.; Small, J. H.; Shea, K. J. *J. Am. Chem. Soc.* **1999**, *121*, 5413.
(29) Liu, W.-C.; Yang, C.-C.; Chen, W.-C.; Dai, B.-T.; Tsai, M.-S. *J. Non-Cryst. Solids* **2002**, *311*, 233.
(30) Matejka, L.; Dukh, O.; Hlavata, D.; Meissner, B.; Brus, J. *Macromolecules* **2001**, *34*, 6904.
(31) Matejka, L.; Dukh, O.; Meissner, B.; Hlavata, D.; Brus, J.; Strachota, A. *Macromolecules* **2003**, *36*, 7977.
(32) Zad, A. I.; Kavei, G.; Tbar, M. R. R.; Allaei, S. M. V. *J. Phys.: Condens. Matter* **2003**, *15*, 1889.
(33) Paze, C.; Bordiga, S.; Zecchina, A. *Langmuir* **2000**, *16*, 8139.
(34) Yang, H.-N.; Wang, G.-C. *J. Appl. Phys.* **1993**, *74*, 101.
(35) Yang, H.-N.; Zhao, Y.-P.; Chan, A.; Lu, T.-M.; Wang, G.-C. *Phys. Rev. Lett.* **1997**, *56*, 4224.
(36) Biscarini, F.; Samori, P.; Greco, O.; Zamboni, R. *Phys. Rev. Lett.* **1997**, *78*, 2389.

MA060573H